

# Deep regression on manifolds: a 3D rotation case study

Romain Brégier  
NAVER LABS Europe  
[www.europe.naverlabs.com](http://www.europe.naverlabs.com)  
[romain.bregier@naverlabs.com](mailto:romain.bregier@naverlabs.com)

## Abstract

*Many problems in machine learning involve regressing outputs that do not lie on a Euclidean space – such as a discrete probability distribution, or the pose of an object. An approach to tackle these problems through gradient-based learning consists in including in the deep learning architecture a differentiable function mapping arbitrary inputs of a Euclidean space onto this manifold. In this work, we establish a set of properties that such mapping should satisfy to allow proper training, and illustrate it in the case of 3D rotations. Through theoretical considerations and methodological experiments on a variety of tasks, we compare various differentiable mappings on the 3D rotation space, and conjecture about the importance of the local linearity of the mapping. We notably show that a mapping based on Procrustes orthonormalization of a  $3 \times 3$  matrix generally performs best among the ones considered, but that rotation-vector representation might also be suitable when restricted to small angles.*

## 1. Introduction

Representations produced by deep neural networks typically consist in arbitrary feature vectors of a Euclidean space. Euclidean spaces however are not suited to represent the output of many problems found in computer vision, for which one might want to regress a point on a specific manifold. Examples include *e.g.* the prediction of a probability distribution for image classification, or the regression of a 3D rotation matrix.

A strategy to overcome this problem consists in designing a differentiable function – such as *softmax* for classification – to map a feature vector onto the manifold and allow the application of deep learning techniques onto this topological space. In this paper, we address this topic while focusing on the special use case of regressing 3D rotations.

**3D rotations** Rigid spatial transformations are an essential concept of many fields ranging from engineering to fundamental physics. In this paper, we study more particularly

the case of 3D rotations and how to regress these using a deep neural network. Regression of 3D rotations arises in many problems of computer vision, such as absolute camera localization [17, 35], object pose estimation [6, 16, 15], parameters identification of a robot kinematic chain or of a human body model [23], or even as an intermediate step of self-supervised depth estimation [36].

The output of a deep learning architecture typically consists in an arbitrary  $n$ -dimensional feature vector  $x$  of a Euclidean space  $X = \mathbb{R}^n$ . However, mapping such arbitrary output to a target manifold  $Y$  such as the 3D rotation space is not trivial, since  $SO(3)$  is not homeomorphic to a Euclidean space. In this context, regressing a rotation using deep learning techniques requires special care and various approaches have been explored to tackle this problem:

**Discretization** One solution consists in discretizing the target space, and reformulate the regression into a classification problem. Such approach has been used with success *e.g.* by [15, 16] for object attitude estimation. It may however not be satisfactory when precise regression is required, as the number of classes required is of the order of  $(1/\alpha^d)$ <sup>1</sup> with respect to the typical discretization length  $\alpha$  and the dimension  $d$  of the target manifold (3 in our case).

**Regression of an intermediary representation** An alternative consists in training the network to regress an intermediary representation using a surrogate loss, and use at test time a procedure to map this representation to an actual element of the target space. In the context of pose estimation from a image, [6] introduced the idea of regressing a set of 2D heat maps representing the 2D projections of 3D keypoints, from which one can estimate a pose at test time by solving a PnP problem. [11] trains similarly a network to regress offsetted 3D keypoints, used at test time to infer a pose. Recently [22] suggested to regress a  $3 \times 3$  matrix representation of a Fischer probability distribution over the space of rotations.

**Differentiable regression on the manifold** A third alternative consists in including a differentiable mapping  $f$  from  $X$  to the target space  $Y$  as an ordinary layer of a deep learning architecture. It can then be trained either to minimize a loss

<sup>1</sup>assuming  $Y$  to be of finite measure.

function expressed on the target domain, or using  $f(\mathbf{x})$  as an unsupervised representation [36].

In this work, we focus on this third alternative. To achieve good training and generalization performances, some constraints have to be satisfied by the mapping used, the choice of which being nontrivial. In a recent paper, Zhou *et al.* [37] proposed a notion of *continuity* to guide this choice. Yet, it suffers from some shortcomings, and we believe that the literature is still lacking a satisfactory explanation about what makes a good mapping function to an arbitrary manifold space for deep learning. In this paper, we aim to contribute to the resolution of this issue. Note that our scope differs from traditional literature on geometric deep learning [2, 3], which focuses on processing data defined on non-Euclidean domain, or characterizing its underlying structure.

**Summary** We formulate in section 2 a set of properties that a mapping onto a manifold should satisfy to be suitable for gradient-based learning, and illustrate it with the example of the *softmax* function. We then review in section 3 a list of existing mappings onto the 3D rotation space and discuss how they satisfy the aforementioned properties. Section 4 consists of experimental studies regarding the regression of 3D rotations, reproducing and extending the work of Zhou *et al.* to other mappings and scenarios. Lastly, we discuss in section 5 the lessons drawn from this work.

## 2. Learning on a differentiable manifold

To train a neural network to output representations on a  $d$ -dimensional manifold  $Y$  through backpropagation, one should define a function  $f : \mathbf{x} \in X \rightarrow f(\mathbf{x}) \in Y$  to map an existing intermediary representation  $\mathbf{x}$  produced by the network and lying on a connected differentiable manifold  $X$  (typically a feature vector of a Euclidean space  $\mathbb{R}^n$ ) to an element  $f(\mathbf{x})$  of  $Y$ . One can then define an arbitrary loss function  $\mathcal{L} = \mathcal{L}(f(\mathbf{x}))$  on the manifold, and perform training as usual, *e.g.* through iterative gradient-descent.

For such mapping to allow proper gradient-based learning, it has to satisfy a set of properties, that we try to establish in this section.

Zhou *et al.* [37] notably states that  $f$  should be surjective. They also propose a notion of *continuity* that would be desirable, which consists in the existence of a continuous right inverse  $g : Y \rightarrow X$ . While such property seems desirable, it consists in our opinion in a very loose criterion. As an example, it is satisfied by the following function from the set of  $3 \times 3$  matrices to the 3D rotation space  $SO(3)$

$$\mathbf{M} \in \mathcal{M}_{3,3}(\mathbb{R}) \rightarrow \begin{cases} \mathbf{M} & \text{if } \mathbf{M} \in SO(3), \\ \mathbf{I} & \text{else.} \end{cases} \quad (1)$$

Yet such mapping is unlikely to be useful in practice, as it maps almost any input to the identity rotation and admits

null derivatives almost everywhere.

### 2.1. Designing a differential mapping

To help in the design or selection of a mapping  $f$ , we establish below a list of properties that  $f$  should satisfy to allow gradient-based learning. The first ones are mandatory for  $f$  to be included in a deep learning framework, whereas the latter ones are desired properties to ensure a proper training.

#### Required properties

##### 0) $Y$ should be a connected differentiable manifold.

Differentiability is indeed required to apply backpropagation during training, and one could not hope reaching an arbitrary target  $y \in Y$  from an arbitrary starting point through small displacements induced by gradient descent if the target space were not composed of a single connected component. Note that a finite set of connected components could be considered nonetheless, by casting regression into a classification problem associated with regression for each of the connected parts.

##### a) $f$ should be surjective, *i.e.* $f(X) = Y$ .

Satisfying this condition is indeed required to be able to predict any arbitrary output  $y \in Y$ .

##### b) $f$ should be differentiable.

This property is required to allow gradient-based optimization, which is the foundation of deep learning. In particular this implies that  $f$  should be continuous.

#### Desired properties

##### c) The Jacobian of $f$ should be of rank $d$ (the dimension of $Y$ ) everywhere.

This property ensures that one can always find an infinitesimal displacement to apply to  $\mathbf{x}$  in order to achieve an arbitrary infinitesimal displacement of the output  $f(\mathbf{x})$ , therefore that there is always a signal to back-propagate during training. In particular, it guarantees convergence of gradient descent towards a global minimum of  $x \rightarrow \mathcal{L}(f(x))$ , when trained with a convex differentiable loss  $\mathcal{L}$  admitting a lower bound. Such guarantee might not be especially important for mappings between high dimensional spaces as there is most of the time a direction in which one can diminish the loss in practice (*e.g.* a ReLU activation layer is a  $\mathbb{R}^n \rightarrow (\mathbb{R}^+)^n$  mapping that does not satisfy this property), but it is more important in the low dimensional regime (*e.g.*  $d = 3$  in the case of 3D rotations).

##### d) The pre-image $f^{-1}(y)$ of any element $y \in Y$ should be connected, or even better, convex.

This property is useful for achieving good training and good generalization. Indeed, consider the case of a backbone network  $h : a \in A \rightarrow x \in X$  producing an intermediate representation  $x$  from an input  $a$ , and a regression problem where one would like to predict a point  $y = f(h(a)) \in Y$  on the target manifold close to a target  $y^* \in Y$ . Training will hopefully bring the representation  $x$  close to an element of the pre-image set  $f^{-1}(y^*)$ . However, due to the

local nature of gradient-descent and the stochastic nature of network initialization and training, different inputs  $a_i \in A$  close to each other and corresponding roughly to the same target output  $y^*$  might produce intermediate representations  $h(a_i) \in X$  that are pushed through gradient-descent towards different elements of  $f^{-1}(y^*)$  far away from each other. It would therefore lead to learning a complex and nearly discontinuous function  $h$ , prone to overfit the training data or to surpass network's capacity. Connectivity constraint on the pre-images of  $f$  mitigates this risk, as it guarantees that optimization will not push representations corresponding to the same output in disconnected regions of the space. Convexity provides even stronger guarantees, as optimization will lead these intermediate representations towards the same convex region, and may therefore enable  $h$  to model a simpler function.

## 2.2. Softmax example

Various existing concepts in traditional deep learning are related to the notions described above. As an example we show how the *softmax* function often used in classification can be thought of as a differentiable function mapping elements of  $X = \mathbb{R}^n$  to a probability distribution  $Y = \{(p_1, \dots, p_n) \in ]0, 1[ \mid \sum_i p_i = 1\}$ . Softmax is defined for a vector  $(x_1, \dots, x_n)$  as follows:

$$\text{softmax}((x_1, \dots, x_n))_i = \frac{\exp(x_i)}{\sum_j \exp(x_j)}. \quad (2)$$

$Y$  consists in a connected  $(n - 1)$ -dimensional manifold on which *softmax* is surjective. It is differentiable with partial derivatives (expressed in ambient space) equal to

$$\frac{\partial p_i}{\partial x_j} = \begin{cases} p_i(1 - p_j) & \text{if } i = j \\ -p_i p_j & \text{else.} \end{cases} \quad (3)$$

The pre-image of any element  $(p_i)_{i=1 \dots n} \in Y$  is convex and consists in a line

$$\text{softmax}^{-1}((p_i)_{i=1 \dots n}) = \{\log(p_i)_{i=1 \dots n} + c \mid c \in \mathbb{R}\}. \quad (4)$$

Therefore, for an arbitrary vector  $\mathbf{x} = (x_i)_{i=1 \dots n}$ , one can choose a given  $c \in \mathbb{R}$  such as  $\log(\text{softmax}(\mathbf{x})) + c = \mathbf{x}$ , applying  $\log$  element-wise. The differentiable function  $g : \mathbf{p} \in Y \rightarrow \log(\mathbf{p}) + c$  can be seen as an inverse of the restriction of  $f$  to  $g(Y)$ , forming a diffeomorphism between  $Y$  and  $g(Y)$  and therefore guaranteeing the Jacobian of  $f$  at  $\mathbf{x}$  to be of same rank as the dimension of  $Y$ .

## 3. Differentiable mappings on $\text{SO}(3)$

Based on the theoretical considerations developed in the last section, we review differentiable functions used in the literature to map arbitrary Euclidean spaces to the 3D rotation space. Table 1 provides a short summary of how these different mappings satisfy the properties listed in section 2.

Table 1. Satisfaction of properties stated in section 2 for mappings onto the 3D rotation space.

	a) surjective	b) differentiable	c) full rank	d) connected pre-image
Euler angles	✓	✓	✗	✗
Rotation vector	✓	✓	✗	✗
Quaternion	✓	✓	✓	✗
6D	✓	✓	✓	✓
Procrustes	✓	✓	✓	✓
Symmetric matrix	✓	✓	✓	✓

**Euler angles** Euler showed in the 18th century [7] that the orientation of any rigid body could be expressed by 3 angles describing a succession of 3 rotations around elementary axes<sup>2</sup>. As an example, one could consider a succession of rotations around respectively the  $x - y - z$  axes and define a mapping

$$(\alpha, \beta, \gamma) \in \mathbb{R}^3 \rightarrow \mathbf{R}_x(\alpha)\mathbf{R}_y(\beta)\mathbf{R}_z(\gamma) \in \text{SO}(3). \quad (5)$$

While being surjective, it does not satisfy the property d) in general due to the existence of multiple discrete pre-images for a given rotation, and its Jacobian suffers from rank deficiency for some rotations (phenomenon referred to as *gimbal lock*). [36] e.g. predicts a 3D translation vector and a rotation parameterized by 3 Euler angles, latter cast into a rigid transformation matrix as part of their unsupervised training strategy.

**Rotation vector** Rotation vectors can be seen as an *un-rolling* of the rotation space on a tangent plane of the identity rotation. Any arbitrary 3D vector can be mapped to the rotation space through the exponential map application (e.g. using Rodrigues' formula), which consists in a surjective function over the rotation space. However, similarly to Euler angles it suffers from multiple discrete pre-images, and rank deficiency for input rotation vectors of angle  $2\pi k$ ,  $k \in \mathbb{N}^*$ . It is used e.g. by [31] to regress parameters of a body model. Note however that a restriction from the open ball of radius  $\alpha < \pi$  to the set of rotations of angle strictly smaller than  $\alpha$  satisfy all the properties of section 2, and that such mapping can therefore be suited to regress rotations of limited angles.

**Non zero quaternion** The rotation group  $\text{SO}(3)$  is diffeomorphic to  $\mathbb{RP}^3$  [9] and therefore one can define a mapping from  $X = \mathbb{R}^4 \setminus \{\mathbf{0}\}$  to  $\text{SO}(3)$  by considering each element  $\mathbf{x} \in X$  as representation of a rotation parameterized by a unit norm quaternion  $\mathbf{q} = \mathbf{x}/\|\mathbf{x}\|$ . Such mapping satisfies all properties a), b) and c) but not d) as the pre-image of any rotation parameterized by a non zero quaternion  $\mathbf{q}$  consists in  $f^{-1}(f(\mathbf{q})) = \{\alpha \mathbf{q} \mid \alpha \in \mathbb{R}^*\}$  which is not connected. This mapping is used e.g. in PoseNet [17] which normalize a 4D vector into a unit quaternion before computing its loss, and [21] suggest a variant of this mapping to stabilize training.

<sup>2</sup>the choice of these being a matter of convention.

**Procrustes** An arbitrary  $3 \times 3$  matrix  $\mathbf{M}$  can also be mapped to the closest rotation matrix in Euclidean space by solving the special orthogonal Procrustes problem

$$\text{Procrustes}(\mathbf{M}) = \arg \min_{\tilde{\mathbf{R}} \in SO(3)} \|\tilde{\mathbf{R}} - \mathbf{M}\|_F^2. \quad (6)$$

Solutions to this minimization problem can be expressed  $\mathbf{USV}^\top$  [33][34], where  $\mathbf{UDV}^\top$  is a singular value decomposition of  $\mathbf{M}$  such that  $\mathbf{U}, \mathbf{V} \in O(d)$ ,  $\mathbf{D} = \text{diag}(\alpha_1, \alpha_2, \alpha_3)$  is a diagonal matrix satisfying  $\alpha_1 \geq \alpha_2 \geq \alpha_3 \geq 0$  and  $\mathbf{S}$  is defined by  $\text{diag}(1, 1, \det(\mathbf{U}) \det(\mathbf{V}))$ . The solution is actually unique if  $\det(\mathbf{M}) > 0$  or  $\alpha_2 \neq \alpha_3$ , and *Procrustes* mapping is therefore well-defined almost everywhere on the set of  $3 \times 3$  matrices, but on a set of null measure (usually ignored in practice). We show in supplementary material that it satisfies all properties presented in section 2, notably that the pre-image of any rotation is convex. *Procrustes* mapping is therefore a suitable candidate for reliable learning, and it can be implemented efficiently for batched GPU applications using off-the-shelf SVD cu-SOLVER routines. It is used *e.g.* in [23] for human pose estimation, and some recent work [20] advocates for its use as a universally effective representation, developing some interesting theoretical arguments complementary to our work.

**6D** Zhou *et al.* [37] proposed a similar approach consisting in mapping a  $3 \times 2$  matrix  $\mathbf{M}$  (6D in total) to a rotation matrix through Gram-Schmidt orthonormalization process. We show in supplementary material that this process can be thought of as a degenerated case of special Procrustes orthonormalization, expressed as a limit

$$6D(\mathbf{M}) = \lim_{\alpha \rightarrow 0^+} \arg \min_{\mathbf{R} \in SO(3)} \|\mathbf{R} \begin{pmatrix} 1 & 0 \\ 0 & \alpha \\ 0 & 0 \end{pmatrix} - \mathbf{M}\|_F^2. \quad (7)$$

Solving this optimization problem for a given  $\alpha > 0$  is equivalent to solving the Procrustes one, considering  $\mathbf{M} \begin{pmatrix} 1 & 0 & 0 \\ 0 & \alpha & 0 \\ 0 & 0 & 0 \end{pmatrix} \in \mathcal{M}_{3,3}(\mathbb{R})$  as input. Both mapping therefore share in that sense similar properties, except that 6D mapping gives importance almost exclusively to the first column of  $\mathbf{M}$  and is well defined when  $\text{rank}(\mathbf{M}) = 2$ . [37] also showed that this 6D representation could actually be compressed into a 5D one through the use of stereographic projection, which led to worse training performances in practice. We show in supplementary material how this mapping satisfy properties of section 2. The 6D mapping is used in various recent papers [27, 19], but concurrent experiments of [20] and ours suggest that it is generally outperformed by Procrustes orthonormalization.

**Symmetric matrix** Lastly, [28] recently proposed to regress 3D rotations as a list of 10 coefficients of a  $4 \times 4$  symmetric matrix  $\mathbf{A}$ , and showed that one could map such matrix to a unique rotation (expressed as a unit quaternion) associated with a particular probability distribution, as long as the

smallest eigenvalue of  $\mathbf{A}$  has a multiplicity of 1. We show in supplementary material how it also satisfies the properties of section 2.

## 4. Experiments

We report in this section a methodological performance evaluation of various mappings to regress 3D rotations in a variety of tasks, namely point cloud alignment (section 4.1), inverse kinematics (section 4.3), camera localization (section 4.3) and object pose estimation (section 4.4). More precisely, we present in sections 4.1 and 4.2 a reproduction and extension of experiments from [37] including an additional mapping *Procrustes*, and studying the variance of the results across multiple trainings. Benchmarks proposed in sections 4.3 and 4.4 are then performed on different tasks. Note that we do not make any novelty claim on the *Procrustes* mapping, but rather want to shed light on its comparative interest with respect to existing ones.

We did not include Euler angles in our experiments, as they do not satisfy the properties presented section 2 and as many different conventions would have to be considered. Similarly, we ignored the mapping based on a  $4 \times 4$  symmetric matrix representation proposed by Peretroukhin *et al.* [28], as the implementation provided by the authors was found too slow to be used in extensive evaluations.

When the loss function used is expressed directly as a distance in  $3 \times 3$  matrix space (sections 4.1 and 4.4), we also evaluate variants consisting in regressing an arbitrary  $3 \times 3$  matrix at training time using this particular loss, and performing the mapping on  $SO(3)$  only at test time (we refer to these variants as *Matrix/Procrustes* and *Matrix/Gram-Schmidt* depending on the mapping used).

### 4.1. Point cloud alignment

We reproduce and extend the experiment of [37] on point clouds alignment, which while being artificial, provides an interesting benchmark.

Given an input 3D point cloud  $C_1 = \{\mathbf{x}_i\}_{i=1 \dots n}$  of size  $n$  (with  $\mathbf{x}_i \in \mathbb{R}^3$ ), and a copy  $C_2 = \{r^*(\mathbf{x}_i)\}_{i=1 \dots n}$  rotated by a random rotation  $r^* \in SO(3)$ , we train a neural network to regress this rotation. The network consists of two Siamese naive PointNets returning a feature vector for each point cloud, which are concatenated and passed through a multi-layer perceptron to output a feature vector  $\mathbf{x} \in \mathbb{R}^n$  mapped to a rotation  $\mathbf{r}$  using one of the studied mappings. Consistently with Zhou *et al.*, training is performed by minimizing the square Frobenius distance between rotation matrices  $\mathbf{R}, \mathbf{R}^* \in \mathcal{M}_{3,3}(\mathbb{R})$  representing these rotations  $r$  and  $r^*$ :

$$\mathcal{L}(r, r^*) = \|\mathbf{R} - \mathbf{R}^*\|_F^2. \quad (8)$$

**Protocol** We follow the protocol of [37], using the dataset provided by the authors representing airplanes from

Table 2. Mean angular error on test set for point cloud alignment, aggregated across 5 independent trainings (lower is better). Subscript and exponent values provided represent respectively the minimal and maximal deviations from the average.

Method	Best validation	Average final error (°)
Rotation vector	12.74°	14.27 <sup>+1.32</sup> <sub>-0.84</sub>
Quaternion	11.66°	12.99 <sup>+1.49</sup> <sub>-1.13</sub>
6D	3.01°	3.47 <sup>+0.45</sup> <sub>-0.45</sub>
<b>Procrustes</b>	<b>2.90°</b>	<b>3.46<sup>+0.59</sup><sub>-0.35</sub></b>
Matrix/Gram-Schmidt	3.66°	4.07 <sup>+0.21</sup> <sub>-0.10</sub>
<b>Matrix/Procrustes</b>	<b>3.33°</b>	<b>3.59<sup>+0.08</sup><sub>-0.09</sub></b>

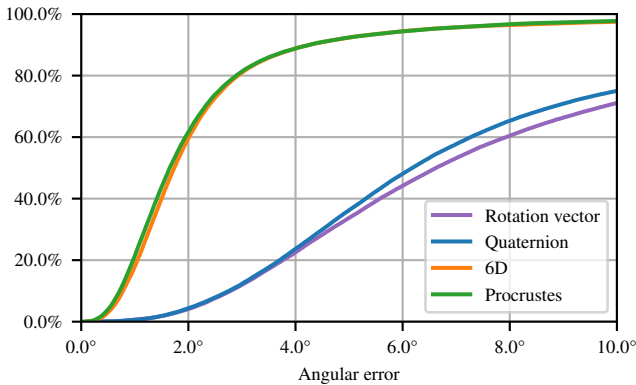


Figure 1. Cumulative angular error distribution on test set for point cloud alignment (best validation models only, for readability).

ShapeNet [5]. We select however randomly a validation set of 400 point clouds from the training data provided, and randomly subsample point clouds to a size of 1024 both at train and test time.

We run the experiment considering various mappings to the rotation space and report results in table 2 and figure 1. Due to the stochastic nature of training, we train/test each variant 5 times and aggregate results to mitigate their variance and increase confidence in our findings. More precisely, we report the error for the model having obtained the smallest validation error (being checked after each training epoch), as well as the final error obtained at the end of training, averaged over 5 runs.

**Results** In accordance with results reported in [37], *rotation vector* and *quaternion* mappings achieve significantly worse performances than the two other mappings. Procrustes orthonormalization leads to better results than Gram-Schmidt, both during training (*Procrustes* vs. *6D*), and when used only at test time (*Matrix/Procrustes* vs. *Matrix/Gram-Schmidt*). Difference of average final error between *Procrustes* and *6D* is too small however to draw clear conclusions from this metric alone, given the deviations observed across the different runs.

Interestingly, we achieve better performance when per-

forming orthonormalization both at training and testing time (*6D* and *Procrustes*) compared to regressing a raw matrix and performing orthonormalization only for validation/test (*Matrix/Gram-Schmidt* and *Matrix/Procrustes*). However, we observe smaller final error variance when training without orthonormalization, with a maximum deviation of 0.18° for *Matrix/Procrustes* vs. 0.91° for *Procrustes*, and 0.31° for *Matrix/Gram-Schmidt* vs. 0.89° for *6D*. We explain this by the fact that learning is more constrained in the direct regression scenario.

## 4.2. Inverse kinematics

We reproduce and extend another experimental setup of [37], more representative of a real use case, and where rotation regression is trained in a self-supervised manner.

The problem consists in learning an inverse kinematic model of a body skeleton illustrated in figure 3, from a set of recorded motions. The forward kinematic function  $f$  mapping the  $n = 57$  rotations  $(r_i)_{i=1 \dots n} \in SO(3)^n$  associated to each joint to the 3D locations  $(\mathbf{x}_i)_{i=1 \dots n} \in \mathbb{R}^{3 \times n}$  of corresponding keypoints is assumed to be known. We train a multi-layer perceptron  $g : \mathbb{R}^{3 \times n} \rightarrow SO(3)^n$  to regress the inverse mapping. During training, given an input list of 3D keypoints locations  $(\mathbf{x}_i^*)_{i=1 \dots n}$ , we use an auto-encoding approach regressing a list of keypoints locations

$$(\mathbf{x}_i)_{i=1 \dots n} = f(g((\mathbf{x}_i^*)_{i=1 \dots n})) \quad (9)$$

and train the network to minimize the square residual

$$\mathcal{L}((\mathbf{x}_i)_{i=1 \dots n}, (\mathbf{x}_i^*)_{i=1 \dots n}) = \sum_{i=1}^n \alpha_i \|\mathbf{x}_i - \mathbf{x}_i^*\|^2. \quad (10)$$

**Protocol** We follow closely the protocol of [37] and use data provided by the authors, consisting in motions from the CMU Motion Capture Database [4]. We select randomly 73 sequences from the training data as validation set, and train each variant with 5 different random weight initialization in order to be able to assess the confidence of our observations.

**Results** We report results obtained in table 3 and figure 2. The two mappings *Procrustes* and *6D* that satisfy the properties of section 2 greatly outperform the two others in this experiment, with *Procrustes* showing significantly better performances than *6D*.

## 4.3. Camera localization

We study the impact of the choice of mapping function on the problem of absolute 6D camera localization, and base our experiments on PoseNet [17], a pioneer work of image-based camera pose regression.

PoseNet processes an input RGB image using a convolutional neural network to regress the camera pose from which

Table 3. Mean per joint position error on the test set for inverse kinematics experiment, aggregated across 5 independent trainings (lower is better). Subscript and exponent values represent respectively the minimal and maximal deviations from the average.

Method	Best validation	Average final error (cm)
Quaternion	1.948cm	$2.208^{+0.208}_{-0.241}$
Rotation vector	1.695cm	$1.840^{+0.102}_{-0.144}$
6D	0.796cm	$0.885^{+0.103}_{-0.079}$
<b>Procrustes</b>	<b>0.721cm</b>	<b>0.795<sup>+0.088</sup><sub>-0.061</sub></b>

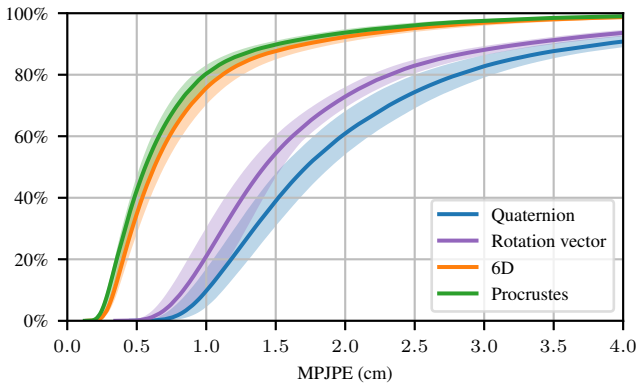


Figure 2. Cumulative mean per joint error distribution on the inverse kinematics test set, aggregated across 5 independent trainings (Solid line: average distribution, shaded areas: maximal deviation across runs).

the image was taken, after a prior supervised training. We rely on the implementation of [35]. In its original version, camera pose is regressed as a pair  $(\mathbf{t}, \mathbf{q})$  composed of a translation vector  $\mathbf{t} \in \mathbb{R}^3$  and a unit quaternion  $\mathbf{q} \in \mathbb{R}^4$  obtained by normalizing an arbitrary 4D output of a neural network. Given a ground truth pose  $(\mathbf{t}^*, \mathbf{q}^*)$ , original training aims to minimize the following cost function

$$\mathcal{L}_{original} = \alpha \|\mathbf{t} - \mathbf{t}^*\|^2 + \beta \gamma \|\mathbf{q} - \mathbf{q}^*\|^2, \quad (11)$$

with  $\alpha = 1/3$ ,  $\gamma = 1/4$  and where  $\beta$  is a scaling factor weighting the importance of rotation *vs.* translation.

**Protocol** We replace the last fully connected layer of the network to produce a feature vector of adequate dimension to apply each evaluated mapping and regress a rotation. Rotation part of the original training loss (11) is actually biased as it is not a valid similarity measure on  $SO(3)$ . Indeed, a given 3D rotation can actually be represented by two antipodal unit quaternions  $\mathbf{q}$  and  $-\mathbf{q}$ , therefore one should instead consider

$$\mathcal{L}_{quaternion} = \alpha \|\mathbf{t} - \mathbf{t}^*\|^2 + \beta \gamma \min \|\mathbf{q} \pm \mathbf{q}^*\|^2 \quad (12)$$

in order to avoid border effects of the representation.

To investigate the impact of this loss function on the results, we also experiment replacing it by one based on the

Frobenius distance between rotation matrices  $\mathbf{R}, \mathbf{R}^*$

$$\mathcal{L}_{Frobenius} = \alpha \|\mathbf{t} - \mathbf{t}^*\|^2 + \beta \delta \|\mathbf{R} - \mathbf{R}^*\|_F^2. \quad (13)$$

We choose  $\delta = \gamma/8$  to weight the two losses similarly (see supplementary material).

We evaluate variants of PoseNet on the *Cambridge Landmarks* datasets, and report the median errors for camera position and orientation. We use hyperparameters provided by Walch *et al.* [35] for each dataset. In accordance with their original work, we do not report results for the *Street* and *Great Court* sets, as training does not converge with the implementation provided. We observed negligible variance in the results across different trainings, because of the use of pretrained weights and deterministic seeding in the implementation, and report therefore a single result for each mapping.

## Results

Results obtained are summarized in table 4.

The baseline *quaternion* mapping trained with the original loss (11) performs well compared to the variants trained with the quaternion loss (12). It is not totally surprising in the sense that hyperparameters have been tuned for this particular setting, introducing a bias in its favor. It notably performs better on average than the *quaternion* mapping trained using loss (12), despite the fact the former is ill-defined on  $SO(3)$  as described previously. We conjecture that it might be due to the combination of two factors. First, loss (12) might be confusing during training and lead to poorer generalization than loss (11) when using a quaternion representation, since gradient-based optimization may push the 4D outputs of the backbone network towards different and opposite regions for two nearby orientations in the case of loss (12) (this relates to the fact that quaternion mapping does not satisfy the pre-image connectivity property introduced in section 2). Second, ground truth unit quaternions representations  $\mathbf{q}^*$  are oriented consistently in the dataset (*e.g.* more than 99% of ground truth quaternions are oriented in the same half-space, for each dataset) and mostly far from the border of the half-space, which mitigates the potential border effects introduced by loss (11).

Results obtained using *Procrustes* representation are globally better than those using *6D* or *quaternion* representations for both losses (12) and (13), and are on average better than the baseline.

Rotation vector representation performed surprisingly well in this experiment despite the fact that this mapping does not satisfy the criteria of section 2, even achieving the best average results for loss (13). We conjecture that this success might be due to a combination of a ‘lucky’ weight initialization and the fact that rotations to regress in the datasets are typically less than  $90^\circ$  away from the identity, enabling the use of a portion of the rotation vector space in which properties of section 2 are roughly met (a similar

Table 4. Median camera localization error on *Cambridge Landmarks* datasets.

Loss	$\mathcal{L}_{original}$	$\mathcal{L}_{quaternion}$ (loss (12))					$\mathcal{L}_{Frobenius}$ (loss (13))				
		quaternion	Rot-vec	6D	Procrustes	Rot-vec 180°	quaternion	Rot-vec	6D	Procrustes	
Representation	quaternion	1.54m, <b>4.25°</b>	1.82m, 4.73°	1.64m, 4.77°	1.64m, 4.82°	<b>1.46m</b> , 5.15°	1.51m, 138.01°	1.87m, 4.98°	<b>1.57m</b> , 4.87°	1.70m, <b>4.56°</b>	1.87m, 5.17°
KingsCollege		2.64m, 5.20°	2.36m, 5.15°	<b>1.95m</b> , 5.88°	2.52m, 4.90°	2.23m, <b>4.63°</b>	2.32m, 155.73°	2.53m, 5.23°	2.56m, 4.97°	2.68m, 4.83°	<b>2.37m</b> , <b>4.39°</b>
OldHospital		<b>2.04m</b> , 10.07°	2.21m, 10.49°	1.44m, 9.68°	2.40m, 10.61°	1.57m, <b>8.25°</b>	1.55m, 143.32°	2.16m, 9.56°	<b>1.27m</b> , <b>7.55°</b>	1.90m, 9.22°	1.50m, 8.75°
ShopFacade		<b>2.06m</b> , <b>7.45°</b>	2.21m, 10.13°	1.94m, 7.88°	2.22m, 8.17°	2.11m, 8.08°	2.02m, 165.23°	<b>1.97m</b> , 8.32°	2.02m, 7.82°	2.14m, 8.01°	2.01m, <b>7.28°</b>
StMarysChurch											
Mean		2.07m, 6.74°	2.15m, 7.63°	<b>1.74m</b> , 7.05°	2.19m, 7.13°	1.84m, <b>6.53°</b>	1.85m, 150.57°	2.13m, 7.02°	<b>1.85m</b> , <b>6.30°</b>	2.10m, 6.65°	1.94m, 6.40°



Figure 3. Experiments illustration. Left: in the inverse kinematics experiment, we try to regress the attitude of joints of a body skeleton given the 3D location of keypoints. Center and right: synthetic and real image crops used in object pose estimation experiment.

hypothesis was studied in [25] for non-monotonic activation functions). We tested this hypothesis by applying to the regressed rotation a 180° rotation around the  $x$  camera axis before loss computation, in such a way that poses to regress are no longer close to the identity. Training completely failed to converge to a good solution for the loss (12), as reported in table 4, which supports our hypothesis. It did however succeed for loss (13), reaching performances of the order of those of the non-rotated version.

#### 4.4. Object pose estimation

Lastly, we investigate the impact of rotation representation for object pose estimation from an RGB image. We focus on regression of object attitude and try to predict the 3D orientation of an object from a  $112 \times 112$  image crop centered around its centroid, illustrated in figure 3.

**Protocol** Experiments are performed on cropped images from the LINEMOD dataset [12], from which we selected randomly for each object 85% of the crops for testing and 15% for validation. We ignore symmetric objects in this evaluation, which are out of the scope of this work (the reader is referred to [32, 1, 29]). Following a common practice [30], we use synthetic data for training, rendering 200,000 crops for each object with randomized pose, illumination and background (as shown figure 3). For the sake of simplicity, we do not use any real data, physically-based renderings, or data-augmentation during training contrary to state-of-the-art methods [14] and cannot therefore pretend reaching the same level of performances. We use for each object a pre-trained ResNet-50 backbone [10], and replace the last fully connected layer by one whose output dimension matches the input dimension of each mapping considered. We freeze the first layers of the backbone (up to the second one) to

speed up training and following insights from [13] regarding generalization performances.

Given a ground truth object orientation expressed as a rotation  $r^* \in SO(3)$ , we train the model to regress a rotation  $r \in SO(3)$  minimizing the mean square distance between paired points of the surface of the object:

$$\mathcal{L}(r, r^*) = \frac{1}{d^2 S} \int_{\mathcal{S}} \|r(\mathbf{x}) - r^*(\mathbf{x})\|^2 ds, \quad (14)$$

where  $\mathcal{S}$  represents the surface of the object<sup>3</sup>, expressed in a coordinate system centered on its centroid,  $S$  its area and where  $d$  is a normalizing factor corresponding to the diameter of the object. Brégier *et al.* [1] showed that the loss (14) admits a closed-form solution  $\|(\mathbf{R} - \mathbf{R}^*)\mathbf{\Lambda}\|_F^2$ , where  $\mathbf{\Lambda}$  is a symmetric positive matrix depending on object geometry. We perform a basic hyperparameter tuning by running for each variant two trainings of 30 epochs with learning rates of 0.1 and 1.0 (respectively of 0.1 and 0.01 for *Matrix/Procrustes* and *Matrix/Gram-Schmidt*) using SGD optimizer, and perform validation after each epoch to select the version to evaluate. At test time, we report the normalized RMS pairwise distance of object points (*i.e.* the square root of the loss), averaged across test examples.

**Results** Experimental results are summarized in table 5. *Procrustes* and *6D* mappings achieve better results than *quaternion* and *rotation-vector* ones, and *Procrustes* outperforms *6D* for most objects. Training to regress an arbitrary  $3 \times 3$  matrix without special orthonormality constraints leads to worse performances at test time, but *Procrustes* orthonormalization still outperforms *Gram-Schmidt* in this scenario.

#### 5. Discussion

In this section, we discuss results of our experiments in the hope to derive some general insight.

We globally observed through our experiments better results achieved with *Procrustes* and *6D* mappings than with the ones based on *quaternion* and *rotation vectors*. These findings are consistent with the theory developed in section 2 about what properties should satisfy a differentiable mapping onto a manifold to enable proper training.

In the camera localization experiment, the drop of performance observed with *quaternion* mapping when switching

<sup>3</sup>described as a triangular mesh in practice.

Table 5. Regression of object orientation from an image patch. Mean RMS pairwise distance of object points, normalized by object diameter (lower is better).

Object	Quat.	Rot-vec	6D	Procr.	Mat/GS.	Mat/Procr.
ape	0.145	0.119	0.085	<b>0.080</b>	0.109	<b>0.107</b>
bench vise	0.062	0.068	0.049	<b>0.042</b>	<b>0.067</b>	0.069
camera	0.139	0.145	0.084	<b>0.067</b>	0.236	<b>0.130</b>
watering can	0.162	0.169	0.134	<b>0.132</b>	0.242	<b>0.239</b>
cat	0.078	0.091	<b>0.048</b>	0.049	0.174	<b>0.111</b>
cup	<b>0.215</b>	0.237	0.219	0.221	0.260	<b>0.232</b>
driller	0.106	0.089	0.059	<b>0.048</b>	0.186	<b>0.144</b>
duck	0.100	0.118	<b>0.050</b>	0.051	0.135	<b>0.129</b>
hole puncher	0.177	0.165	0.137	<b>0.126</b>	0.218	<b>0.176</b>
iron	0.051	0.053	0.041	<b>0.037</b>	<b>0.055</b>	0.079
lamp	0.061	0.054	<b>0.032</b>	0.035	0.088	<b>0.081</b>
phone	0.101	0.129	<b>0.073</b>	0.077	0.155	<b>0.122</b>
Mean	0.116	0.120	0.084	<b>0.080</b>	0.160	<b>0.135</b>

from the original PoseNet loss (11) to a well-defined loss on the rotation space (12) supports the idea that the non-connectivity of pre-images is a problem for learning. It is somehow also supported by the failure to converge to a low error solution observed with rotation-vector representation.

We observed that regressing a  $3 \times 3$  matrix and performing *Procrustes* orthonormalization at training time globally performed better than using the *6D* representation. Work concurrent to ours [37] led to similar conclusions and provides two arguments. The first consists in the smaller sensitivity of *Procrustes* orthonormalization to Gaussian noise compared to Gram-Schmidt, but their results only hold locally for perturbations applied to a rotation matrix. The second is that *Procrustes* orthonormalization is left and right invariant to rotations, whereas Gram-Schmidt is only left-invariant (we discussed in section 3 how Gram-Schmidt was giving more importance to its first input column vector). While these are meaningful considerations, we offer here as another explanation that the *Procrustes* mapping is more ‘linear’ than *6D* and *quaternion* mappings for typical input ranges, and we support this claim by numerical experiments.

To this aim, we draw for each mapping  $\mathbf{R} : \mathbf{x} \in \mathbb{R}^n \rightarrow \mathbf{R}(\mathbf{x}) \in SO(3)$  some random input vector  $\mathbf{x} \sim \mathcal{N}(0, 1)^n$ , as well as some unit 3D vectors  $\mathbf{v}_1, \mathbf{v}_2$  of uniform random direction. Because of the way *Procrustes*, *6D* and *quaternion* mappings are defined,  $\mathbf{R}(\mathbf{x})$  is uniformly distributed over  $SO(3)$  and no directional bias is introduced by this approach. We define a loss function  $\mathcal{L}(\mathbf{x}) = \mathbf{v}_1^T \mathbf{R}(\mathbf{x}) \mathbf{v}_2$ , estimate its gradient  $\nabla \mathcal{L}_{\mathbf{x}}$  and compute for a given step size  $\epsilon > 0$  the absolute deviation from the linear case:

$$|\mathcal{L}(\mathbf{x} - \epsilon \nabla \mathcal{L}_{\mathbf{x}}) - (\mathcal{L}(\mathbf{x}) - \epsilon \|\nabla \mathcal{L}_{\mathbf{x}}\|^2)|. \quad (15)$$

Results for various step sizes are plotted in figure 4 and illustrate *Procrustes*’ better linearity over the two others.

We also observed that using a differentiable mapping  $\mathbf{x} \rightarrow f(\mathbf{x})$  at training time and defining a loss on the target manifold performed better in our experiments than training to regress a representation  $\mathbf{x}$ , and mapping it to the manifold

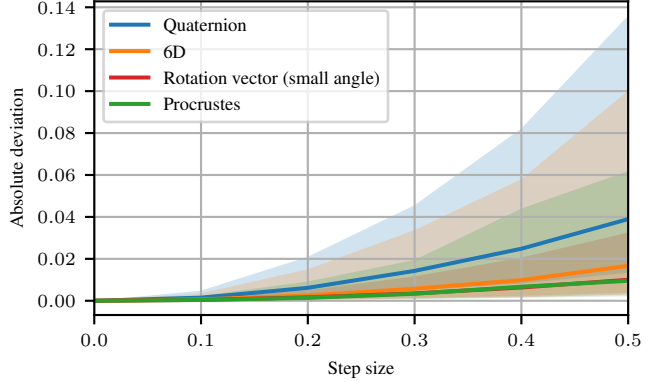


Figure 4. Deviation from linearity of different mappings on  $SO(3)$  (solid curves: median, shaded areas: 25%-75% percentiles). Curve corresponding to *Rotation vector* is masked by *Procrustes*.

at test time (e.g. *Procrustes* vs. *Matrix/Procrustes*). This seems a natural finding as we optimize in the former case an objective function corresponding to our actual goal, defined on the manifold, whereas the latter case considers only a surrogate objective in representation space.

Finally, our experiments with PoseNet showed that rotation vectors could perform well in some circumstances, and notably when considering rotations of limited angle. Rotation-vector mapping actually satisfies the criteria of section 2 when restricted from a unit ball of radius  $r \in ]0, \pi[$  to the corresponding set of rotations, and the plot in figure 4 suggests a similar linearity between *Procrustes* and the mapping to rotations of angle strictly smaller than  $\pi/2$

$$\mathbf{x} \in \mathbb{R}^3 \rightarrow \exp \left( \frac{\pi}{2} \tanh(\|\mathbf{x}\|) \frac{\mathbf{x}}{\|\mathbf{x}\|} \right) \quad (16)$$

for normal inputs<sup>4</sup>.

## 6. Conclusion

In this paper, we study the problem of learning to regress elements on a manifold, through the use of a differentiable mapping from the Euclidean output space of a neural network to this manifold. We establish a list of properties that such mapping should satisfy to allow a proper training through gradient-based optimization, and study more specifically the case of the 3D rotation manifold. We consider some existing mappings both from a theoretical and experimental standpoint, and suggest that linearity might be an important additional aspect to achieve good learning performances. We notably find that a mapping based on special *Procrustes* orthonormalization performs best among the mappings considered when regressing arbitrary rotations, but that rotation-vector representations may be as well suited when the output can be constrained to limited rotation angles.

<sup>4</sup>Comparison makes sense as the normal distribution used to sample  $\mathbf{x}$  enables a reasonably good coverage of the output space of mapping (16).

Table 6. Value of PoseNet hyperparameter  $\beta$  for the different datasets.

King's College	500
OldHospital	1500
Shop Facade	100
St Mary's Church	250

## 7. Supplementary material

Section A provides some technical details regarding the experiments, and section B provides proofs regarding mathematical statements contained in the paper.

### A. Experimental details

Experiments were implemented using PyTorch 1.6 [26].

#### A.1. Point cloud alignment

We follow closely the protocol of [37]. Rotations are sampled uniformly according to the usual  $SO(3)$  metric both for training and testing. Sizes of training, validation and test sets are respectively 1890, 400, 400. We train the network with a batch size of 10 for  $2.6 \cdot 10^6$  iterations, using Adam optimizer [18] with a learning rate of  $10^{-4}$ . 100 rotations are considered for each point cloud during test. We train each variant with 5 different random weight initialization.

#### A.2. Inverse kinematics

We use the provided test set (73 sequences, 107,119 poses), but split randomly the training sequences into a validation (73 sequences, 116,427 poses) and training set (721 sequences, 1,030,236 poses). We train the network using Adam optimizer with a learning rate of  $10^{-5}$  and a batch size of 64 for 1,960k iterations.

In accordance with the reference implementation of Zhou *et al.* [37], hyperparameters  $\alpha_i$  introduced in equation (10) of the paper are defined equal to  $1/(3n)$  for all keypoints but 3 corresponding to the hips and for which  $\alpha_i = 1/(3n) + 10/9$ , where  $n$  denotes the number of keypoints. We train each variant with 5 different random weight initialization.

#### A.3. Camera localization

We choose  $\delta = \gamma/8$  to weight the losses  $\mathcal{L}_{Frobenius}$  and  $\mathcal{L}_{quaternion}$  similarly, based on the following identities relative to the angle  $\alpha$  between two rotations [1]:

$$\left\{ \begin{array}{l} \min \|\mathbf{q} \pm \mathbf{q}^*\|^2 = 4 \sin^2(\alpha/4) \underset{\alpha \rightarrow 0}{\sim} \alpha^2/4 \\ \|\mathbf{R} - \mathbf{R}^*\|_F^2 = 8 \sin^2(\alpha/2) \underset{\alpha \rightarrow 0}{\sim} 2\alpha^2. \end{array} \right. \quad (17)$$

Values for the hyperparameter  $\beta$  are listed in table 6 and correspond to the ones suggested in the PoseNet implementation of Walch *et al.* [35].

## B. Proofs of paper's statements

We sketch in this section proofs of mathematical statements from the paper, especially regarding

- rotation vector representation (section B.2).
- Procrustes mapping (section B.3).
- Gram-Schmidt mapping (section B.4).
- $4 \times 4$  symmetric matrix representation (section B.5).
- the restriction of rotation vector representation to small angles (section B.6).

### B.1. Useful lemma

Let  $f$  be a differentiable function between two differentiable manifolds  $X$  and  $Y$ , and let  $d$  be the dimension of  $Y$ .

For  $x \in X$ , if there exists a submanifold  $A \subset X$  containing  $x$  and for which the restriction  $f|_A$  is a diffeomorphism from  $A$  to  $Y$ , then the Jacobian of  $f$  is of rank  $d$  at  $x$ .

**Proof** Since  $f|_A$  is a diffeomorphism to a  $d$ -dimensional manifold, its Jacobian is of rank  $d$ , therefore the rank of the Jacobian of  $f$  in  $x$  is at least  $d$ . But its rank is also at most  $d$ , since the image of  $f$  is within  $Y$ .

### B.2. Rotation vector

Rotation vector space corresponds to the usual Lie algebra associated to  $SO(3)$ . As such, it is well known that the exponential mapping

$$f : \mathbf{x} \in \mathbb{R}^3 \rightarrow \exp(\mathbf{x}) \in SO(3) \quad (18)$$

is surjective, continuous and differentiable.

The pre-image of a rotation parameterized by  $\mathbf{x} \in \mathbb{R}^3$  consists in

$$f^{-1}(f(\mathbf{x})) = \begin{cases} \left\{ \left( 1 + \frac{2\pi k}{\|\mathbf{x}\|} \right) \mathbf{x} \mid k \in \mathbb{Z} \right\} & \text{if } \|\mathbf{x}\| \neq 0. \\ \{\mathbf{0}\} \cup \{\mathbf{v} \in \mathbb{R}^3 \mid \|\mathbf{v}\| \in 2\pi\mathbb{Z}^*\} & \text{else.} \end{cases} \quad (19)$$

which is not connected.

In particular, for  $\mathbf{x}$  of norm  $2\pi k$ , with  $k \in \mathbb{N}^*$ , the pre-image of  $f(\mathbf{x})$  restricted to a small neighborhood of  $\mathbf{x}$  consists in a 2D-manifold (a subset of a sphere going through  $\mathbf{x}$ ), therefore  $f$  is not locally invertible at  $\mathbf{x}$  and its Jacobian cannot therefore be of rank 3 (the dimension of  $\mathbb{R}^3$  and  $SO(3)$ ) at  $\mathbf{x}$ . This result can also be obtained by observing an analytical expression of the derivatives of  $f$  (replacing *e.g.*  $\mathbf{v}$  by  $(2\pi, 0, 0)^\top$  in equation (III.1) of [8], and observing the rank deficiency).

**Restriction to a ball of limited angle.** Given an arbitrary angle  $\alpha \in ]0, \pi[$ , the restriction of exponential map from the open ball of radius  $\alpha \{x \in \mathbb{R}^3 | \|x\| < \alpha\}$  to the set of rotations of angle strictly smaller than  $\alpha$  is a diffeomorphism. It therefore satisfies properties of surjectivity, differentiability, full rank Jacobian and connected pre-image proposed in section 2 of the paper.

### B.3. Special Procrustes orthonormalization

Given  $d \in \mathbb{N}$  with  $d \geq 2$ , and a  $d \times d$  matrix  $\mathbf{M} \in \mathcal{M}_{d,d}(\mathbb{R})$ , we consider the special orthogonal Procrustes problem consisting in finding the  $d \times d$  rotation matrix  $\mathbf{R} \in SO(d)$  closest to  $\mathbf{M}$

$$\mathbf{R} = \arg \min_{\tilde{\mathbf{R}} \in SO(3)} h(\mathbf{M}, \tilde{\mathbf{R}}), \quad (20)$$

considering the square Frobenius distance

$$h(\mathbf{M}, \tilde{\mathbf{R}}) = \|\tilde{\mathbf{R}} - \mathbf{M}\|_F^2. \quad (21)$$

Solutions to this problem consist in  $\mathbf{U}\mathbf{S}\mathbf{V}^\top$  [33][34], where  $\mathbf{U}\mathbf{D}\mathbf{V}^\top$  is a singular value decomposition of  $\mathbf{M}$  such that  $\mathbf{U}, \mathbf{V} \in O(d)$ ,  $\mathbf{D} = \text{diag}(d_1, \dots, d_d)$  is a diagonal matrix verifying

$$d_1 \geq \dots \geq d_d \geq 0, \quad (22)$$

and such that  $\mathbf{S} = \text{diag}(1, \dots, 1, \det(\mathbf{U}) \det(\mathbf{V}))$ .

The solution is unique if and only if  $\det(\mathbf{M}) > 0$  or  $d_{d-1} \neq d_d$ . We will denote  $X$  the set of input matrices  $\mathbf{M}$  satisfying this property and Procrustes the function mapping any  $\mathbf{M} \in X$  to the corresponding solution of the special Procrustes problem (20).

#### B.3.1 Surjectivity

For any  $\mathbf{R} \in SO(d)$ , one can verify that  $X$  contains  $\mathbf{R}$  and that  $\text{Procrustes}(\mathbf{R}) = \mathbf{R}$ . This proves the surjectivity of the Procrustes mapping.

#### B.3.2 Differentiability

Let  $\mathbf{M} = (m_{ij})_{ij} \in X$  and  $\mathbf{R} = \text{Procrustes}(\mathbf{M})$ .

Papadopoulou and Lourakis [24] showed how SVD decomposition could be locally differentiated, and we build upon their work to provide an analytical expression of the derivatives of Procrustes in the ambient space  $\mathcal{M}_{d,d}(\mathbb{R})$ .

Using notations introduced in the beginning of section B.3,

$$\mathbf{R} = \mathbf{U}\mathbf{S}\mathbf{V}^\top \quad (23)$$

and therefore for any  $i, j \in \llbracket 1, d \rrbracket$ ,

$$\frac{\partial \mathbf{R}}{\partial m_{ij}} = \frac{\partial \mathbf{U}}{\partial m_{ij}} \mathbf{S}\mathbf{V}^\top + \mathbf{U} \frac{\partial \mathbf{S}}{\partial m_{ij}} \mathbf{V}^\top + \mathbf{U} \mathbf{S} \left( \frac{\partial \mathbf{V}}{\partial m_{ij}} \right)^\top. \quad (24)$$

Since  $\mathbf{S}$  is locally constant (being equal either to  $\text{diag}(1, \dots, 1)$  or  $\text{diag}(1, \dots, -1)$ ), its partial derivatives are null, therefore

$$\frac{\partial \mathbf{R}}{\partial m_{ij}} = \frac{\partial \mathbf{U}}{\partial m_{ij}} \mathbf{S}\mathbf{V}^\top + \mathbf{U} \mathbf{S} \left( \frac{\partial \mathbf{V}}{\partial m_{ij}} \right)^\top. \quad (25)$$

Since  $\mathbf{U}, \mathbf{V} \in O(d)$ , their partial derivatives have to encode this orthogonality constraint and can therefore be written

$$\begin{cases} \frac{\partial \mathbf{U}}{\partial m_{ij}} = \mathbf{U} \boldsymbol{\Omega}_U^{ij} \\ \frac{\partial \mathbf{V}}{\partial m_{ij}} = -\mathbf{V} \boldsymbol{\Omega}_V^{ij}, \end{cases} \quad (26)$$

introducing  $\boldsymbol{\Omega}_U^{ij}$  and  $\boldsymbol{\Omega}_V^{ij}$  two skew-symmetric matrices (see [24] for details).

Hence, partial derivative can be rewritten

$$\frac{\partial \mathbf{R}}{\partial m_{ij}} = \mathbf{U} \boldsymbol{\Omega}_U^{ij} \mathbf{V}^\top \quad (27)$$

with  $\boldsymbol{\Omega}^{ij} = (\boldsymbol{\Omega}_U^{ij} \mathbf{S} + \mathbf{S} \boldsymbol{\Omega}_V^{ij})$ .

Papadopoulou and Lourakis [24] showed that elements of  $\boldsymbol{\Omega}_U^{ij}$  and  $\boldsymbol{\Omega}_V^{ij}$  satisfy a particular set of linear equations.

Solving this system (while accounting for the potential flip of sign induced by  $\mathbf{S}$ ) enables to provide an analytical expression for the elements of  $\boldsymbol{\Omega}^{ij}$ :

$$\boldsymbol{\Omega}_{kl}^{ij} = \begin{cases} 0 & \text{if } k = l. \\ \frac{u_{ik}v_{jl} - u_{il}v_{jk}}{d_k - d_l} & \text{if } l = d, k \neq d \text{ and } \det(\mathbf{U}) \det(\mathbf{V}) < 0. \\ \frac{u_{ik}v_{jl} - u_{il}v_{jk}}{d_l - d_k} & \text{if } k = d, l \neq d \text{ and } \det(\mathbf{U}) \det(\mathbf{V}) < 0. \\ \frac{u_{ik}v_{jl} - u_{il}v_{jk}}{d_l + d_k} & \text{else.} \end{cases} \quad (28)$$

Since  $\det(\mathbf{M}) = \det(\mathbf{U}) \det(\mathbf{D}) \det(\mathbf{V})$  and since  $\det(\mathbf{D}) \geq 0$ , we consider two different cases to show that the denominator does not cancel out in this expression:

If  $\det(\mathbf{M}) > 0$ , then  $\det(\mathbf{U}) \det(\mathbf{V}) > 0$  and  $d_1 \geq \dots \geq d_d > 0$ , therefore elements of  $\boldsymbol{\Omega}^{ij}$  are well-defined.

If  $\det(\mathbf{M}) \leq 0$ , then  $\det(\mathbf{U}) \det(\mathbf{V}) < 0$  and  $d_d \neq d_{d-1}$  by definition of  $X$ . Therefore  $d_1 \geq \dots \geq d_{d-1} > d_d$  and elements of  $\boldsymbol{\Omega}^{ij}$  are also well-defined.

We obtain a closed-form expression of the partial derivative of *Procrustes* by injecting this expression of  $\boldsymbol{\Omega}^{ij}$  in equation (27).

#### B.3.3 Full rank Jacobian

Let  $\mathbf{M} \in X$  and  $\mathbf{R} = \text{Procrustes}(\mathbf{M})$ . The function

$$g_{\mathbf{M}} : \tilde{\mathbf{R}} \in SO(d) \rightarrow \mathbf{M}\mathbf{R}^\top \tilde{\mathbf{R}} \quad (29)$$

is differentiable and is the inverse of the restriction of Procrustes from  $g_M(SO(d))$  to  $SO(d)$ , *i.e.* for any  $\tilde{\mathbf{R}} \in SO(d)$ ,

$$\text{Procrustes}(g_M(\tilde{\mathbf{R}})) = \text{Procrustes}(\mathbf{M}) \mathbf{R}^\top \tilde{\mathbf{R}} = \tilde{\mathbf{R}}. \quad (30)$$

Procrustes is therefore a diffeomorphism from  $g_M(SO(d))$  to  $SO(d)$  and its Jacobian is thus of rank  $d$  (the dimension of  $SO(d)$  manifold) according to lemma B.1.

### B.3.4 Pre-image convexity

Equation (21) can be developed using a trace operator into

$$h(\mathbf{M}, \tilde{\mathbf{R}}) = \|\mathbf{M}\|_F^2 + \|\tilde{\mathbf{R}}\|_F^2 - 2 \text{Tr}(\mathbf{M} \tilde{\mathbf{R}}^\top). \quad (31)$$

Since  $\tilde{\mathbf{R}}$  is a rotation matrix, this expression is equivalent to

$$h(\mathbf{M}, \tilde{\mathbf{R}}) = \|\mathbf{M}\|_F^2 + \|\mathbf{I}\|_F^2 - 2 \text{Tr}(\mathbf{M} \tilde{\mathbf{R}}^\top). \quad (32)$$

where  $\mathbf{I}$  denotes the  $d \times d$  identity matrix.

Minimizing

$$\tilde{\mathbf{R}} \in SO(d) \rightarrow h(\mathbf{M}, \tilde{\mathbf{R}}) \quad (33)$$

is therefore equivalent to maximizing

$$\tilde{\mathbf{R}} \in SO(d) \rightarrow \text{Tr}(\mathbf{M} \tilde{\mathbf{R}}^\top). \quad (34)$$

Let  $\mathbf{R} \in SO(d)$ , and  $\mathbf{M}_1, \mathbf{M}_2 \in X$  two pre-images of  $\mathbf{R}$  by Procrustes, *i.e.*

$$\text{Procrustes}(\mathbf{M}_1) = \text{Procrustes}(\mathbf{M}_2) = \mathbf{R}. \quad (35)$$

By definition,  $\mathbf{R}$  is the unique rotation maximizing the function defined in equation (34), considering  $\mathbf{M} = \mathbf{M}_1$  and  $\mathbf{M} = \mathbf{M}_2$ . For any  $\alpha, \beta \in \mathbb{R}^{+*}$ , thanks to the linearity of matrix multiplication and trace operator,  $\mathbf{R}$  is therefore the unique maximizer of the function defined in equation (34) considering  $\mathbf{M} = \alpha \mathbf{M}_1 + \beta \mathbf{M}_2$  *i.e.*

$$\text{Procrustes}(\alpha \mathbf{M}_1 + \beta \mathbf{M}_2) = \mathbf{R}. \quad (36)$$

This proves in particular the convexity of the pre-image of  $\mathbf{R}$  by Procrustes.

## B.4. Special Gram-Schmidt orthonormalization

### B.4.1 Gram-Schmidt process

The Gram-Schmidt process enables to generate an orthonormal  $n$ -tuple of  $d$ -dimensional vectors  $(\mathbf{e}_1, \dots, \mathbf{e}_n)$  from a linearly independent  $n$ -tuple of  $d$ -dimensional vectors  $(\mathbf{v}_1, \dots, \mathbf{v}_n)$  (assuming  $n \leq d$ ). It is defined iteratively by  $\mathbf{e}_1 = \mathbf{v}_1 / \|\mathbf{v}_1\|$  and

$$\mathbf{e}_k = \left( \mathbf{v}_k - \sum_{j=1}^{k-1} \text{proj}_{\mathbf{e}_j}(\mathbf{v}_k) \right) / \left\| \mathbf{v}_k - \sum_{j=1}^{k-1} \text{proj}_{\mathbf{e}_j}(\mathbf{v}_k) \right\| \quad (37)$$

for  $k = 2 \dots n$ , where  $\text{proj}$  denotes the projection operator defined by

$$\text{proj}_{\mathbf{a}}(\mathbf{b}) = \frac{\mathbf{a}^\top \mathbf{b}}{\|\mathbf{a}\|^2} \cdot \mathbf{a} \quad (38)$$

for any pair of vectors  $\mathbf{a}, \mathbf{b} \in \mathbb{R}^d$  with  $\mathbf{a} \neq \mathbf{0}$ .

### B.4.2 Special Gram-Schmidt orthonormalization

Let  $d \in \mathbb{N}$  with  $d \geq 2$ . We define

$$X = \{ \mathbf{V} \in \mathcal{M}_{d,d-1}(\mathbb{R}) \mid \text{rank}(\mathbf{V}) = d-1 \} \quad (39)$$

the set of  $d \times (d-1)$  matrices  $\mathbf{V}$  whose column vectors  $(\mathbf{v}_1, \dots, \mathbf{v}_{d-1})$  are linearly independent.

We denote GramSchmidt the mapping from  $X$  to  $SO(d)$  defined for any  $\mathbf{V} = (\mathbf{v}_1, \dots, \mathbf{v}_{d-1}) \in X$  by

$$\text{GramSchmidt}(\mathbf{V}) = (e_1 \ \dots \ e_d) \quad (40)$$

where the  $(e_i)_{i=1, \dots, d-1}$  are defined as in equation (37) and where  $e_d$  is chosen as the unique vector such that  $\text{GramSchmidt}(\mathbf{V}) \in SO(d)$ .

For  $d = 3$ , GramSchmidt corresponds to the 6D mapping of Zhou *et al.* [37], in which case  $e_3$  can be defined by  $e_3 = e_1 \times e_2$ .

### B.4.3 Surjectivity

For any  $\mathbf{R} \in SO(d)$ , the matrix  $(\mathbf{r}_1, \dots, \mathbf{r}_{d-1})$  composed of the first  $(d-1)$  columns of  $\mathbf{R}$  belongs to  $X$  and

$$\text{GramSchmidt}((\mathbf{r}_1, \dots, \mathbf{r}_{d-1})) = \mathbf{R}. \quad (41)$$

This proves the surjectivity of GramSchmidt.

### B.4.4 Differentiability

All operations of the special Gram-Schmidt orthonormalization process are differentiable on  $X$ , and we can therefore deduce the differentiability of GramSchmidt on  $X$ .

### B.4.5 Full rank Jacobian

Let  $\mathbf{V} \in X$  and  $\mathbf{R} = \text{GramSchmidt}(\mathbf{V})$ . The function

$$g_{\mathbf{V}} : \tilde{\mathbf{R}} \in SO(d) \rightarrow \tilde{\mathbf{R}} \mathbf{R}^{-1} \mathbf{V} \in X \quad (42)$$

is differentiable and for any  $\tilde{\mathbf{R}} \in SO(d)$ ,

$$\begin{aligned} \text{GramSchmidt}(g_{\mathbf{V}}(\tilde{\mathbf{R}})) &= \tilde{\mathbf{R}} \mathbf{R}^{-1} \text{GramSchmidt}(\mathbf{V}) \\ &= \tilde{\mathbf{R}}. \end{aligned} \quad (43)$$

The restriction of GramSchmidt from  $g_{\mathbf{V}}(SO(d))$  to  $SO(d)$  is therefore a diffeomorphism, from which we conclude that the rank of GramSchmidt Jacobian at  $\mathbf{V}$  is  $d$  (the dimension of  $SO(d)$  manifold), from lemma B.1.

#### B.4.6 Pre-image convexity

Let  $\mathbf{A}, \mathbf{B} \in X$  having the same image

$$\text{GramSchmidt}(\mathbf{A}) = \text{GramSchmidt}(\mathbf{B}) = \mathbf{E} \in SO(d). \quad (44)$$

We denote respectively  $(\mathbf{a}_1, \dots, \mathbf{a}_{d-1}), (\mathbf{b}_1, \dots, \mathbf{b}_{d-1})$  and  $(\mathbf{e}_1, \dots, \mathbf{e}_d)$  the column vectors of  $\mathbf{A}, \mathbf{B}$ , and  $\mathbf{E}$ .

Let  $\alpha, \beta \in \mathbb{R}^{+*}$  be two strictly positive scalars. We prove in this section that

$$\text{GramSchmidt}(\alpha\mathbf{A} + \beta\mathbf{B}) = \mathbf{E}. \quad (45)$$

It implies in particular that the pre-image of  $\mathbf{E}$  by GramSchmidt is convex.

**Proof** Let  $(\mathbf{c}_1, \dots, \mathbf{c}_d)$  be the column vectors of  $\text{GramSchmidt}(\alpha\mathbf{A} + \beta\mathbf{B})$ .

By definition,

$$\mathbf{e}_1 = \frac{\mathbf{a}_1}{\|\mathbf{a}_1\|} = \frac{\mathbf{b}_1}{\|\mathbf{b}_1\|} \quad (46)$$

which implies that  $\mathbf{a}_1$  and  $\mathbf{b}_1$  are non-zero collinear vectors pointing in the same direction.  $\alpha\mathbf{a}_1 + \beta\mathbf{b}_1$  is consequently also a non-null vector aligned with  $\mathbf{e}_1$ , therefore

$$\mathbf{e}_1 = \frac{\alpha\mathbf{a}_1 + \beta\mathbf{b}_1}{\|\alpha\mathbf{a}_1 + \beta\mathbf{b}_1\|} = \mathbf{c}_1. \quad (47)$$

Let  $k \in \llbracket 2, d-1 \rrbracket$  such that for all  $j \in \llbracket 1, k-1 \rrbracket$ ,  $\mathbf{e}_j = \mathbf{c}_j$ . Since  $\text{proj}$  is a linear operator, the following equalities hold true:

$$\begin{aligned} & \alpha\mathbf{a}_k + \beta\mathbf{b}_k - \sum_{j=1}^{k-1} \text{proj}_{\mathbf{c}_j}(\alpha\mathbf{a}_j + \beta\mathbf{b}_j) \\ &= \alpha\mathbf{a}_k + \beta\mathbf{b}_k - \sum_{j=1}^{k-1} \text{proj}_{\mathbf{e}_j}(\alpha\mathbf{a}_j + \beta\mathbf{b}_j) \\ &= \underbrace{\alpha \left( \mathbf{a}_k - \sum_{j=1}^{k-1} \text{proj}_{\mathbf{e}_j}(\mathbf{a}_j) \right)}_{\mathbf{f}} + \beta \underbrace{\left( \mathbf{b}_k - \sum_{j=1}^{k-1} \text{proj}_{\mathbf{e}_j}(\mathbf{b}_j) \right)}_{\mathbf{g}}. \end{aligned} \quad (48)$$

From the definition of  $\mathbf{e}_k$ , we know that underbraced terms  $\mathbf{f}$  and  $\mathbf{g}$  consist in non-null vectors aligned with  $\mathbf{e}_k$ .  $\alpha\mathbf{f} + \beta\mathbf{g}$  is therefore a non-null vector aligned with  $\mathbf{e}_k$  as well and consequently

$$\mathbf{c}_k = \frac{\alpha\mathbf{f} + \beta\mathbf{g}}{\|\alpha\mathbf{f} + \beta\mathbf{g}\|} = \mathbf{e}_k. \quad (49)$$

This proves by induction that  $\mathbf{e}_k = \mathbf{c}_k$  for any  $k \in \llbracket 1, d-1 \rrbracket$ .

Since  $\mathbf{c}_d$  only depends on  $(\mathbf{c}_k)_{k=1 \dots d-1}$ , we deduce that  $\mathbf{c}_d = \mathbf{e}_d$ , which concludes the proof.

#### B.4.7 Lemma: weighted special Procrustes orthonormalization

Let  $\mathbf{M}, \mathbf{\Lambda} \in \mathcal{M}_{d,n}(\mathbb{R})$  be two arbitrary  $d \times n$  matrices (considering an arbitrary  $n \in \mathbb{N}^*$ ). Minimizing the function

$$\mathbf{R} \in SO(d) \rightarrow \|\mathbf{R}\mathbf{\Lambda} - \mathbf{M}\|_F^2 \quad (50)$$

is equivalent to minimizing

$$\mathbf{R} \in SO(d) \rightarrow \|\mathbf{R} - \mathbf{M}\mathbf{\Lambda}^\top\|_F^2. \quad (51)$$

**Proof** For any  $\mathbf{R} \in SO(d)$ ,

$$\|\mathbf{R}\mathbf{\Lambda} - \mathbf{M}\|_F^2 = \|\mathbf{\Lambda}\|_F^2 + \|\mathbf{M}\|_F^2 - 2 \text{Tr}(\mathbf{R}\mathbf{\Lambda}\mathbf{M}^\top) \quad (52)$$

and

$$\|\mathbf{R} - \mathbf{M}\mathbf{\Lambda}^\top\|_F^2 = \|\mathbf{I}\|_F^2 + \|\mathbf{M}\mathbf{\Lambda}^\top\|_F^2 - 2 \text{Tr}(\mathbf{R}\mathbf{\Lambda}\mathbf{M}^\top). \quad (53)$$

Both expressions are equal up to a constant with respect to  $\mathbf{R}$ . Minimizing one with respect to  $\mathbf{R}$  is therefore equivalent to minimizing the other.

#### B.4.8 Link between Gram-Schmidt and Procrustes

We denote  $(\mathbf{\Lambda}_n)_{n \in \mathbb{N}}$  a series of  $d \times (d-1)$  matrices

$$\mathbf{\Lambda}_n = \begin{pmatrix} \lambda_{1,n} & 0 & 0 \\ 0 & \ddots & 0 \\ 0 & 0 & \lambda_{d-1,n} \\ 0 & 0 & 0 \end{pmatrix} \quad (54)$$

satisfying for any  $n \in \mathbb{N}$

$$\begin{cases} \lambda_{1,n} = 1 \\ \lambda_{i,n} > 0 \text{ for } i = 1, \dots, d-1 \end{cases} \quad (55)$$

and defined such that  $\lambda_{i,n} = o(\lambda_{i-1,n})$  for  $i \in \llbracket 2, d-1 \rrbracket$ , using Landau notations.

For  $\mathbf{M} \in X$ , we show in this section that if the series  $(\text{Procrustes}(\mathbf{M}\mathbf{\Lambda}_n^\top))_{n \in \mathbb{N}}$  converges, its limit consists in  $\text{GramSchmidt}(\mathbf{M})$ .

**Proof** Let  $n \in \mathbb{N}$ ,  $\mathbf{M} \in X$  and  $\mathbf{R} \in SO(d)$ . We denote  $(\mathbf{r}_1, \dots, \mathbf{r}_d)$  and  $(\mathbf{m}_1, \dots, \mathbf{m}_{d-1})$  the respective column vectors of  $\mathbf{R}$  and  $\mathbf{M}$ . We denote

$$E(\mathbf{R}, \mathbf{\Lambda}_n) = \|\mathbf{R}\mathbf{\Lambda}_n - \mathbf{M}\|_F^2 \quad (56)$$

the minimization problem to which  $\text{Procrustes}(\mathbf{M}\mathbf{\Lambda}_n^\top)$  is associated (see lemma B.4.7).  $\text{Procrustes}(\mathbf{M}\mathbf{\Lambda}_n^\top)$  is well defined because  $\text{rank}(\mathbf{M}\mathbf{\Lambda}_n^\top) = d-1$ , therefore the smallest singular value of  $\mathbf{M}\mathbf{\Lambda}_n^\top$  is 0 with a multiplicity of 1.

It is straightforward to show that for any  $j \in \llbracket 1, d-1 \rrbracket$ ,

$$\begin{aligned} E(\mathbf{R}, \Lambda_n) &= \|\mathbf{M}\|^2 + \sum_{i=1}^{d-1} \lambda_{i,n}^2 - 2 \sum_{i=1}^{d-1} \lambda_{i,n} \mathbf{r}_i^\top \mathbf{m}_i \\ &= \|\mathbf{M}\|^2 + \sum_{i=1}^j \lambda_{i,n}^2 - 2 \sum_{i=1}^j \lambda_{i,n} \mathbf{r}_i^\top \mathbf{m}_i + o(\lambda_{j,n}). \end{aligned} \quad (57)$$

In particular, for  $j = 1$ ,

$$E(\mathbf{R}, \Lambda_n) = \|\mathbf{M}\|^2 + 1 - 2\mathbf{r}_1^\top \mathbf{m}_1 + o(1). \quad (58)$$

Assuming that  $(\text{Procrustes}(\mathbf{M}\Lambda_n^\top))_{n \in \mathbb{N}}$  admits a limit  $\mathbf{R}^* = (\mathbf{r}_1^* \dots \mathbf{r}_d^*) \in SO(d)$ , this limit should tend to minimize equation (58), i.e. maximize  $\mathbf{r}_1^\top \mathbf{m}_1$ . Therefore  $\mathbf{r}_1^*$  should be equal to  $\mathbf{m}_1 / \|\mathbf{m}_1\|$ .

Similarly, assuming that the expressions of  $\mathbf{r}_1^*, \dots, \mathbf{r}_{j-1}^*$  are known for a given  $j \in \llbracket 1, d-1 \rrbracket$ ,  $\mathbf{R}^*$  should tend to minimize equation (57), i.e. tend to maximize  $\mathbf{r}_j^\top \mathbf{m}_j$ , which is obtained for

$$\mathbf{r}_j^* = \left( \mathbf{m}_j - \sum_{i=1}^{j-1} \text{proj}_{\mathbf{r}_i^*}(\mathbf{m}_j) \right) / \left\| \mathbf{m}_j - \sum_{i=1}^{j-1} \text{proj}_{\mathbf{r}_i^*}(\mathbf{m}_j) \right\|. \quad (59)$$

A limit of  $(\text{Procrustes}(\mathbf{M}\Lambda_n^\top))_{n \in \mathbb{N}}$  should therefore correspond to the special Gram-Schmidt orthonormalization of  $\mathbf{M}$ .

## B.5. Symmetric matrix

For  $\mathbf{a} = (a_1, \dots, a_{10})^\top \in \mathbb{R}^{10}$ , we denote  $\mathbf{S}_a$  the  $4 \times 4$  symmetric matrix

$$\mathbf{S}_a = \begin{pmatrix} a_1 & a_2 & a_3 & a_4 \\ a_2 & a_5 & a_6 & a_7 \\ a_3 & a_6 & a_8 & a_9 \\ a_4 & a_7 & a_9 & a_{10} \end{pmatrix}. \quad (60)$$

Let  $\mathbf{V} \text{diag}(\lambda_1, \dots, \lambda_4) \mathbf{V}^\top$  an eigenvalue decomposition of  $\mathbf{S}_a$ , with  $\mathbf{V} \in O(4)$  the matrix of eigenvectors and  $\lambda_1, \dots, \lambda_4$  the corresponding eigenvalues, sorted in ascending order.

The optimization problem proposed by Peretroukhin *et al.* [28]

$$\min_{\mathbf{q} \in \mathbb{R}^4 / \|\mathbf{q}\|=1} \mathbf{q}^\top \mathbf{S}_a \mathbf{q} \quad (61)$$

admits a unique pair of antipodal solutions  $\pm \mathbf{q}$  if and only if  $\lambda_1 \neq \lambda_2$ , and this solution  $\mathbf{q}$  consists in the first column vector of  $\mathbf{V}$ , corresponding to the eigenvector associated with the smallest eigenvalue  $\lambda_1$ .

Let  $X \subset \mathbb{R}^{10}$  be the set of vectors  $\mathbf{a}$  for which a minimizer  $\mathbf{q}$  of (61) is unique (up to sign), and let  $\text{SymMatrix} : X \rightarrow \mathbb{RP}^3$  denote the function mapping  $\mathbf{a}$  to  $\mathbf{q}$ .

Peretroukhin *et al.* [28] showed that this mapping was surjective and differentiable, and proposed an expression of its Jacobian. We show in the next subsections how it satisfies properties regarding the rank of its Jacobian and the connectivity of its pre-images.

### B.5.1 Full rank Jacobian

Let  $\mathbf{a} \in X$  and  $\mathbf{q} = \text{SymMatrix}(\mathbf{a})$  a corresponding unit quaternion.

For any unit quaternion  $\tilde{\mathbf{q}} = w + xi + yj + zk \in \mathbb{RP}^3$ , we denote

$$\mathbf{M}_{\tilde{\mathbf{q}}} = \begin{pmatrix} w & -x & -y & -z \\ x & w & -z & y \\ y & z & w & -x \\ z & -y & x & w \end{pmatrix} \in O(4) \quad (62)$$

a matrix representation of  $\tilde{\mathbf{q}}$ , and we define the function

$$g_{\mathbf{a}} : \tilde{\mathbf{q}} \in \mathbb{RP}^3 \rightarrow \mathbf{M}_{\tilde{\mathbf{q}}^{-1}}^\top \mathbf{M}_{\tilde{\mathbf{q}}}^\top \mathbf{S}_a \mathbf{M}_{\tilde{\mathbf{q}}} \mathbf{M}_{\tilde{\mathbf{q}}^{-1}}. \quad (63)$$

$g_{\mathbf{a}}$  is well-defined, as  $g_{\mathbf{a}}(\tilde{\mathbf{q}}) = g_{\mathbf{a}}(-\tilde{\mathbf{q}})$  for any  $\tilde{\mathbf{q}} \in \mathbb{RP}^3$ . It returns symmetric matrices whose eigenvalues are identical to those of  $\mathbf{S}_a$ , and for any unit quaternions  $\tilde{\mathbf{q}}, \mathbf{q}^*$ ,

$$\begin{aligned} \pm \mathbf{q}^* &= \text{SymMatrix}(g_{\mathbf{a}}(\tilde{\mathbf{q}})) \\ \Leftrightarrow \pm \mathbf{M}_{\mathbf{q}} \mathbf{M}_{\tilde{\mathbf{q}}^{-1}} \mathbf{q}^* &= \text{SymMatrix}(\mathbf{S}_a) \\ \Leftrightarrow \pm \tilde{\mathbf{q}} \tilde{\mathbf{q}}^{-1} \mathbf{q}^* &= \pm \mathbf{q} \\ \Leftrightarrow \pm \mathbf{q}^* &= \pm \tilde{\mathbf{q}}. \end{aligned} \quad (64)$$

Identifying a symmetric matrix with its vectorized entries, the range of  $g_{\mathbf{a}}$  is therefore included in  $X$ , and  $g_{\mathbf{a}}$  is the differentiable inverse of the restriction of  $\text{SymMatrix}$  from  $g_{\mathbf{a}}(\mathbb{RP}^3)$  to  $\mathbb{RP}^3$ . We conclude that the Jacobian of  $\text{SymMatrix}$  is of rank 3 (the dimension of  $\mathbb{RP}^3$  manifold) at  $\mathbf{a}$  using lemma B.1.

### B.5.2 Pre-image convexity

Let  $\mathbf{a}, \mathbf{b} \in X$  and  $\pm \mathbf{q}^* \in \mathbb{RP}^3$  such that

$$\text{SymMatrix}(\mathbf{a}) = \text{SymMatrix}(\mathbf{b}) = \pm \mathbf{q}^*. \quad (65)$$

For any  $\alpha, \beta \in \mathbb{R}^{+*}$ , both functions

$$\mathbf{q} \in \mathbb{R}^4 / \|\mathbf{q}\|=1 \rightarrow \alpha \mathbf{q}^\top \mathbf{S}_a \mathbf{q} \quad (66)$$

and

$$\mathbf{q} \in \mathbb{R}^4 / \|\mathbf{q}\|=1 \rightarrow \beta \mathbf{q}^\top \mathbf{S}_b \mathbf{q} \quad (67)$$

admit a unique pair of minimizers  $\pm \mathbf{q}^* \pm \mathbf{q}^*$  are therefore also the only minimizers of

$$\mathbf{q} \in \mathbb{R}^4 / \|\mathbf{q}\|=1 \rightarrow \mathbf{q}^\top (\alpha \mathbf{S}_a + \beta \mathbf{S}_b) \mathbf{q}. \quad (68)$$

We deduce that  $\alpha \mathbf{a} + \beta \mathbf{b} \in X$  and  $\text{SymMatrix}(\alpha \mathbf{a} + \beta \mathbf{b}) = \pm \mathbf{q}^*$ . In particular, it implies that the pre-image set  $\text{SymMatrix}^{-1}(\pm \mathbf{q}^*)$  is convex.

## B.6. Limited range rotation vector

Given  $n \in \mathbb{N}^*$  and  $\alpha \in \mathbb{R}^{++}$ , we denote  $B_\alpha$  the open ball of  $\mathbb{R}^n$  of radius  $\alpha$ .

The function

$$g_\alpha : \mathbf{x} \in \mathbb{R}^n \rightarrow \alpha \frac{\tanh(\|\mathbf{x}\|)}{\|\mathbf{x}\|} \mathbf{x} \in B_\alpha \quad (69)$$

extended by  $g_\alpha(\mathbf{0}) = \mathbf{0}$  is continuous and differentiable everywhere, with partial derivatives equal to

$$\begin{cases} \frac{\partial g_{\alpha,i}}{\partial x_i} = \alpha \left( -\frac{x_i^2 \tanh(\|\mathbf{x}\|)}{\|\mathbf{x}\|^3} + \frac{\tanh(\|\mathbf{x}\|)}{\|\mathbf{x}\|} + \frac{x_i^2 \operatorname{sech}^2(\|\mathbf{x}\|)}{\|\mathbf{x}\|^2} \right) \\ \frac{\partial g_{\alpha,i}}{\partial x_j} = \alpha \left( \frac{x_i x_j \operatorname{sech}^2(\|\mathbf{x}\|)}{\|\mathbf{x}\|^2} - \frac{x_i x_j \tanh(\|\mathbf{x}\|)}{\|\mathbf{x}\|^3} \right) \text{ for } i \neq j. \end{cases} \quad (70)$$

Taylor series expansion show the continuity of  $g_\alpha$  and its derivatives in  $\mathbf{0}$ , which are locally equivalent to

$$\begin{cases} g_\alpha(\mathbf{x}) \sim \alpha \mathbf{x} \\ \frac{\partial g_{\alpha,i}}{\partial x_i} \sim \alpha \left( 1 - \frac{5}{6} x_i^2 \right) \\ \frac{\partial g_{\alpha,i}}{\partial x_j} \sim -\frac{2}{3} \alpha x_i x_j \text{ for } i \neq j. \end{cases} \quad (71)$$

$g_\alpha$  admits moreover a differentiable inverse

$$g_\alpha^{-1} : \mathbf{y} \in B_\alpha \rightarrow \frac{\tanh^{-1}(\|\mathbf{y}\|/\alpha)}{\|\mathbf{y}\|} \mathbf{y} \quad (72)$$

and is therefore a diffeomorphism from  $\mathbb{R}^n$  to  $B_\alpha$ .

Considering  $n = 3$  and  $\alpha \in ]0, \pi[$ , the exponential map  $\exp$  is a diffeomorphism from  $B_\alpha$  to the manifold of 3D rotations of angle strictly smaller than  $\alpha$ . The composed function  $g_\alpha \circ \exp$  is therefore a diffeomorphism from  $\mathbb{R}^n$  to this set of rotations, and it therefore satisfies properties of surjectivity, differentiability, full rank Jacobian and pre-image connectivity proposed in section 2 of the paper.

## References

- [1] Romain Brégier, Frédéric Devernay, Laetitia Leyrit, and James L. Crowley. Defining the Pose of Any 3D Rigid Object and an Associated Distance. *International Journal of Computer Vision*, 2018. [7](#) [9](#)
- [2] Michael M. Bronstein, Joan Bruna, Yann LeCun, Arthur Szlam, and Pierre Vandergheynst. Geometric deep learning: going beyond Euclidean data. *IEEE Signal Processing Magazine*, 2017. [2](#)
- [3] W. Cao, Z. Yan, Z. He, and Z. He. A Comprehensive Survey on Geometric Deep Learning. *IEEE Access*, 2020. [2](#)
- [4] CMU Graphics Lab Motion Capture Database. <http://mocap.cs.cmu.edu>. [5](#)
- [5] Angel X. Chang, Thomas Funkhouser, Leonidas Guibas, Pat Hanrahan, Qixing Huang, Zimo Li, Silvio Savarese, Manolis Savva, Shuran Song, Hao Su, Jianxiong Xiao, Li Yi, and Fisher Yu. ShapeNet: An Information-Rich 3D Model Repository. Technical Report arXiv:1512.03012 [cs.GR], 2015. [5](#)
- [6] Alberto Crivellaro, Mahdi Rad, Yannick Verdie, Kwang Moo Yi, Pascal Fua, and Vincent Lepetit. A novel representation of parts for accurate 3d object detection and tracking in monocular images. In *ICCV*, 2015. [1](#)
- [7] Leonhard Euler. Formulae generales pro translatione quacunque corporum rigidorum. *Euler Archive - All Works by Eneström Number*, 1776. [3](#)
- [8] Guillermo Gallego and Anthony Yezzi. A compact formula for the derivative of a 3-D rotation in exponential coordinates. *Journal of Mathematical Imaging and Vision*, (3):378–384, 2015. [9](#)
- [9] Brian C. Hall. *Lie Groups, Lie Algebras, and Representations: An Elementary Introduction*, Graduate Texts in Mathematics, 222 (2nd ed.). Springer, 2015. [3](#)
- [10] Kaiming He, Xiangyu Zhang, Shaoqing Ren, and Jian Sun. Deep residual learning for image recognition. In *CVPR*, 2016. [7](#)
- [11] Yisheng He, Wei Sun, Haibin Huang, Jianran Liu, Haoqiang Fan, and Jian Sun. PVN3D: A Deep Point-Wise 3D Keypoints Voting Network for 6DoF Pose Estimation. In *CVPR*, 2020. [1](#)
- [12] Stefan Hinterstoisser, Stefan Holzer, Cedric Cagniart, Slobodan Ilic, Kurt Konolige, Nassir Navab, and Vincent Lepetit. Multimodal templates for real-time detection of texture-less objects in heavily cluttered scenes. In *ICCV*, 2011. [7](#)
- [13] Stefan Hinterstoisser, Vincent Lepetit, Paul Wohlhart, and Kurt Konolige. On Pre-Trained Image Features and Synthetic Images for Deep Learning. In *ECCV*, 2018. [7](#)
- [14] Tomas Hodan, Martin Sundermeyer, Bertram Drost, Yann Labbe, Eric Brachmann, Frank Michel, Carsten Rother, and Jiri Matas. BOP Challenge 2020 on 6D Object Localization. In *ECCVW*, 2020. [7](#)
- [15] Asako Kanezaki, Yasuyuki Matsushita, and Yoshifumi Nishida. RotationNet: Joint Object Categorization and Pose Estimation Using Multiviews from Unsupervised Viewpoints. In *CVPR*, 2018. [1](#)
- [16] Wadim Kehl, Fabian Manhardt, Federico Tombari, Slobodan Ilic, and Nassir Navab. SSD-6D: Making RGB-Based 3D Detection and 6D Pose Estimation Great Again. In *ICCV*, 2017. [1](#)
- [17] Alex Kendall, Matthew Grimes, and Roberto Cipolla. PoseNet: A convolutional network for real-time 6-DOF camera relocalization. In *ICCV*, 2015. [1](#), [3](#), [5](#)
- [18] Diederik P. Kingma and Jimmy Ba. Adam: A Method for Stochastic Optimization. In *ICLR*, 2015. [9](#)
- [19] Muhammed Kocabas, Nikos Athanasiou, and Michael J. Black. VIBE: Video Inference for Human Body Pose and Shape Estimation. In *CVPR*, 2020. [4](#)
- [20] Jake Levinson, Carlos Esteves, Kefan Chen, Angjoo Kanazawa, Afshin Rostamizadeh, Noah Snavely, and Ameesh Makadia. An Analysis of SVD for Deep Rotation Estimation. In *NeurIPS*, 2020. [4](#)
- [21] Shuai Liao, Efstratios Gavves, and Cees G. M. Snoek. Spherical Regression: Learning Viewpoints, Surface Normals and 3D Rotations on n-Spheres. In *CVPR*, 2019. [3](#)

[22] D. Mohlin, G. Bianchi, and J. Sullivan. Probabilistic orientation estimation with matrix Fisher distributions. *NeurIPS*, 2020. 1

[23] Mohamed Omran, Christoph Lassner, Gerard Pons-Moll, Peter V. Gehler, and Bernt Schiele. Neural Body Fitting: Unifying Deep Learning and Model-Based Human Pose and Shape Estimation. In *3DV*, 2018. 1, 4

[24] Théodore Papadopoulo and Manolis I. A. Lourakis. Estimating the Jacobian of the Singular Value Decomposition: Theory and Applications. In *ECCV*, 2000. 10

[25] Giambattista Parascandolo, Heikki Huttunen, and Tuomas Virtanen. Taming the waves: sine as activation function in deep neural networks. 2016. 7

[26] Adam Paszke, Sam Gross, Francisco Massa, Adam Lerer, James Bradbury, Gregory Chanan, Trevor Killeen, Zeming Lin, Natalia Gimelshein, Luca Antiga, Alban Desmaison, Andreas Kopf, Edward Yang, Zachary DeVito, Martin Raison, Alykhan Tejani, Sasank Chilamkurthy, Benoit Steiner, Lu Fang, Junjie Bai, and Soumith Chintala. Pytorch: An imperative style, high-performance deep learning library. In *Advances in Neural Information Processing Systems*, 2019. 9

[27] Georgios Pavlakos, Nikos Kolotouros, and Kostas Daniilidis. TexturePose: Supervising Human Mesh Estimation with Texture Consistency. In *ICCV*, 2019. 4

[28] Valentin Peretroukhin, Matthew Giamou, David M. Rosen, W. Nicholas Greene, Nicholas Roy, and Jonathan Kelly. A Smooth Representation of Belief over  $SO(3)$  for Deep Rotation Learning with Uncertainty. In *Robotics: Science and Systems XVI*, 2020. 4, 13

[29] Giorgia Pitteri, Michael Ramamonjisoa, Slobodan Ilic, and Vincent Lepetit. On Object Symmetries and 6D Pose Estimation from Images. In *3DV*, 2019. 7

[30] Mahdi Rad and Vincent Lepetit. BB8: A Scalable, Accurate, Robust to Partial Occlusion Method for Predicting the 3D Poses of Challenging Objects without Using Depth. In *ICCV*, 2017. 7

[31] Yu Rong, Ziwei Liu, Cheng Li, Kaidi Cao, and Chen Change Loy. Delving Deep Into Hybrid Annotations for 3D Human Recovery in the Wild. In *ICCV*, 2019. 3

[32] A. Saxena, J. Driemeyer, and A.Y. Ng. Learning 3-D object orientation from images. In *ICRA*, 2009. 7

[33] Peter H. Schönemann. A generalized solution of the orthogonal Procrustes problem. *Psychometrika*, 1966. 4, 10

[34] Shinji Umeyama. Least-squares estimation of transformation parameters between two point patterns. *TPAMI*, 1991. 4, 10

[35] F. Walch, C. Hazirbas, L. Leal-Taixe, T. Sattler, S. Hilsenbeck, and D. Cremers. Image-Based Localization Using LSTMs for Structured Feature Correlation. In *ICCV*, 2017. 1, 6, 9

[36] Tinghui Zhou, Matthew Brown, Noah Snavely, and David G Lowe. Unsupervised Learning of Depth and Ego-Motion From Video. In *CVPR*, 2017. 1, 2, 3

[37] Yi Zhou, Connelly Barnes, Jingwan Lu, Jimei Yang, and Hao Li. On the Continuity of Rotation Representations in Neural Networks. In *CVPR*, 2019. 2, 4, 5, 8, 9, 11